

Lawrence Berkeley National Laboratory  
LBL Publications

Title

Decoupling Complex Multi-Length-Scale Morphology in Non-Fullerene Photovoltaics with Nitrogen K-Edge Resonant Soft X-ray Scattering

Permalink

<https://escholarship.org/uc/item/592363d9>

Journal

Advanced Materials, 34(6)

ISSN

0935-9648

Authors

Zhong, Wenkai  
Zhang, Ming  
Freychet, Guillaume  
et al.

Publication Date

2022-02-01

DOI

10.1002/adma.202107316

Peer reviewed

# **Visualizing Complex Multi-Length-Scale Morphology in Non-Fullerene Photovoltaics with Nitrogen K-Edge Resonant Soft X-Ray Scattering**

Wenkai Zhong, Ming Zhang, Guillaume Freychet, Gregory M. Su, Lei Ying, Fei Huang, Yong Cao, Yongming Zhang, Cheng Wang,\* Feng Liu\*

**ABSTRACT:** Multi-length-scale morphology in organic photovoltaics (OPVs) and other functional soft materials leads to high complexity, but often dictates functionality. Such mesoscale complexity in OPVs originates from the kinetically trapped nonequilibrium morphology, which determines the charge generation and transport of the resultant device. Resonant soft x-ray scattering (RSoXS) has been revolutionary on the exploration of OPV morphology in the past decade. However, for non-fullerene OPVs, RSoXS analysis near carbon K-edge (CK-RSoXS) has been difficult, due to the similar carbon-based frameworks in the materials used in bulk-heterojunction blends. An innovative approach is provided by nitrogen K-edge RSoXS (NK-RSoXS), utilizing the spatial and orientational contrasts from the cyano groups in the acceptor material, which allows for determination of the phase separation. Of particular importance is that NK-RSoXS, for the first time, clearly visualizes the combined morphology in PM6:Y6 blends originated from crystallization and spinodal phase separation, yielding feature sizes that dictate optoelectronic properties. NK-RSoXS also reveals that PM6:Y6:BO ternary blends with reduced phase separation size and enhanced material crystallization can lead to current amplification in devices. Nitrogen is common in organic semiconductors and other soft materials, and the strong and directional N 1s $\rightarrow\pi^*$  resonances make NK-RSoXS a unique tool to uncover mesoscale complexity and opens opportunities to understand heterogeneous systems.

## INTRODUCTION

The functionality of materials is strongly correlated with the collective assembly of active entities beyond the chemical construction. This phenomenon is highlighted in soft materials where the structure is complex and the mesoscale behavior that bridge chemistry and assembly plays an important role in dictating material performance.<sup>1,2</sup> Control over the molecular assembly on multiscale and mesoscale requires not only a fundamental understanding of the material properties, but also viable and efficient metrology that can quantitatively resolve and analyze the complex structure associated with diverse functions. To characterize the mesoscale phenomena spanning multiple spatial and temporal scales, element-sensitive resonance soft x-ray scattering (RSoXS) provides a chemical label-free solution to resolve the internal complexity of phase separation and interfacial orientation for a range of functional soft materials.<sup>3- 10</sup> The scattering contrast of RSoXS stems from the complex index of refraction,  $n(E) = 1 - \delta(E) + i\beta(E)$ , where  $\delta(E)$  and  $\beta(E)$  are the dispersion and imaginary parts, respectively. Thus, contrast with chemical sensitivity can be achieved since  $\delta$  and  $\beta$  change substantially as a function of energy near absorption edges. The contrast function,  $\Delta\delta^2 + \Delta\beta^2$ , can be used to evaluate different phases quantitatively.<sup>9-11</sup>

Organic photovoltaics (OPVs) active layers illustrate the complexity in multicomponent soft materials. The mixing and phase separation between donor (D) and acceptor (A) materials determine the charge generation and transport, as well as the power conversion efficiency of devices.<sup>12- 14</sup> Carbon K-edge RSoXS (CK-RSoXS) has been proven to be a successful tool to study phase separated blends comprised of  $\pi$ -conjugated donors and fullerene acceptors, where the fullerene exhibits high resonance arising from  $1s(C=C) \rightarrow \pi^*_{C=C}$  transitions at  $\sim 284.2$  eV.<sup>15- 18</sup> However, the structure-property relationship in emerging non-fullerene acceptor (NFA) based D/A blends that deliver higher efficiencies are difficult to quantify due to the challenges in achieving high scattering contrast.<sup>19- 23</sup> The chemical similarity between D and A leads to comparable and superposed near edge x-ray absorption fine structure (NEXAFS) spectral features at the C K-edge, impeding the chemical sensitivity of CK-RSoXS. Meanwhile, conventional microscopic techniques, such as transmission electron microscopy (TEM) and atomic force microscopy (AFM) are less effective, as the materials have similar electron densities and surface mechanical properties.<sup>24</sup>

To address these challenges, we leverage nitrogen K-edge RSoXS (NK-RSoXS) by utilizing the nitrogen (N) absorption features in the materials.<sup>19,20</sup> In organic semiconductors, N-based

groups influence the optical and electronic properties for  $\pi$ -conjugated polymers and small molecules. From a chemistry perspective, the  $sp^2$  hybridized N atoms in hetero-aromatic rings confer different coordinating properties depending on the bonding environment, which lead to well-defined NEXAFS features that can be explored. For example, the lone pair of electrons in the 2p orbital of the N bridge in carbazole or dithieno[3,2-*b*:2',3'-*d*]pyrrole can delocalize across the conjugated plane, enhancing the electron-donating capability of these units.<sup>25</sup> On the contrary, the lone pairs of  $sp^2$  orbitals for N atoms in a C=N bond in fused rings, such as benzo[*d*][1,2,3]triazole, benzo[*c*][1,2,5]thiadiazole, and pyridal[2,1,3]thiadiazole, quinoxaline, localize around the N atoms, resulting in strong electron-withdrawing characteristics.<sup>26-30</sup> A unique case is the cyano group, where the C≡N has an sp hybridized N atom that forms two  $\pi$  bonds with two pairs of orthogonal p orbitals, and a localized lone pair yielding large electronegativity.<sup>19,20,31-36</sup> Therefore, nitrogen is an important chemical element in  $\pi$ -conjugated polymers and small molecules, which enables NK-RSoXS to provide new opportunities in revealing the mesoscale structure chemically and spatially in organic semiconductor thin films and other disciplines.

## RESULTS AND DISCUSSION

The viability of NK-RSoXS in characterizing the phase separation in non-fullerene D/A blends for OPVs is demonstrated. The D/A combination PBDBT:ITIC (1:1 by weight) blend was chosen (Figure 1a). ITIC is an A-D-A type NFA, where the cyano groups are incorporated for increasing the electronegativity of A groups, leading to strong absorbance in the near-infrared (NIR) region that contributes to high OPV power conversion efficiency.<sup>37</sup> For the cyano group, the C≡N is composed of one  $\sigma$  bond and two  $\pi$  bonds, where the  $\pi$  bonds are formed from two pairs of p orbitals ( $p_y$  and  $p_z$ ) that are orthogonal to each other. The N K-edge NEXAFS spectral analysis of ITIC was conducted to study the energy-dependent chemical resonance associated with N atoms. As shown in Figure 1b, the NEXAFS of ITIC shows three absorption peaks at 398.8 eV, 400.2 eV, and 401.5 eV, which are labeled with “A”, “B”, and “C”. Angle-dependent NEXAFS reveals that as the incident angle,  $\theta$ , increases, the intensities of peak A and peak C deceases, while the peak B intensity increases. This suggests that the transition dipole moments (TDMs) for transitions A and C are perpendicular to B. Since ITIC has been shown to assume a “face-on” orientation on the substrate,<sup>38,39</sup> it is expected that the TDMs for peaks A and C are normal to the conjugated plane, and the TDM for peak B is in the conjugated plane.

More detailed chemical and electronic origins for these peaks are investigated by NEXAFS simulations using first-principles calculations based on the excited electron and core hole (XCH) approach.<sup>40,41</sup> To simplify the calculation, the side chains and aromatic ring indacenodithieno[3,2-*b*]thiophene (IDTT) were replaced by methyl groups and indacenodithiophene (IDT), respectively. As shown in Figure 1c, the simulated NEXAFS displays a profile with three spectral features, labeled with “A”, “B”, and “C”, consistent with the experimental data. Compared with experiment, there is a discrepancy in the energy position of B relative to A and C in the simulation, which may be due to these Perdew-Burke-Ernzerhof (PBE) calculations cannot accurately describe the highly localized  $\pi^*$  states in the system.<sup>41</sup> However, the directionality of B relative to A and C is reproduced in the simulations, so it is convinced that the theory captures the electronic origins of these key features. The core-excited final-state orbitals corresponding to the resonant absorption of A and C show that these features correspond to N 1s  $\rightarrow \pi^*(p_z)$  transitions, as seen by positive and negative regions of the wavefunction above and below the aromatic rings, which confirms that their TDMs point normal to the conjugated plane (see the side views shown in Figure S2). The orbital corresponding to the resonant absorption of feature B shows  $\pi$  symmetry with respect to the internuclear axis of C and N, and parallel to the conjugated plane, indicating the resonance is from N 1s  $\rightarrow \pi^*(p_y)$  transitions with TDM within conjugated plane. One notes that the orbitals of A and C are delocalized over the conjugated plane, while orbital of B is localized around the cyano group. This suggests the  $\pi$  bond formed from the  $p_z$  orbitals can well couple into the delocalized  $\pi$  systems, which is further verified by the simulated core-excited final state orbitals of C 1s  $\rightarrow \pi^*$  transitions from the cyano group (Figure S3). The x-, y-, and z-components of the simulated spectra were extracted, showing that features A and C are dominated by the z-component, while feature B is contributed by x- and y-components (Figure S4). Since the conjugated plane of the model molecule is parallel to the x-y plane, the results are in good agreement with the absorption dichroism for peaks A/C and peak B observed in angle-dependent NEXAFS.

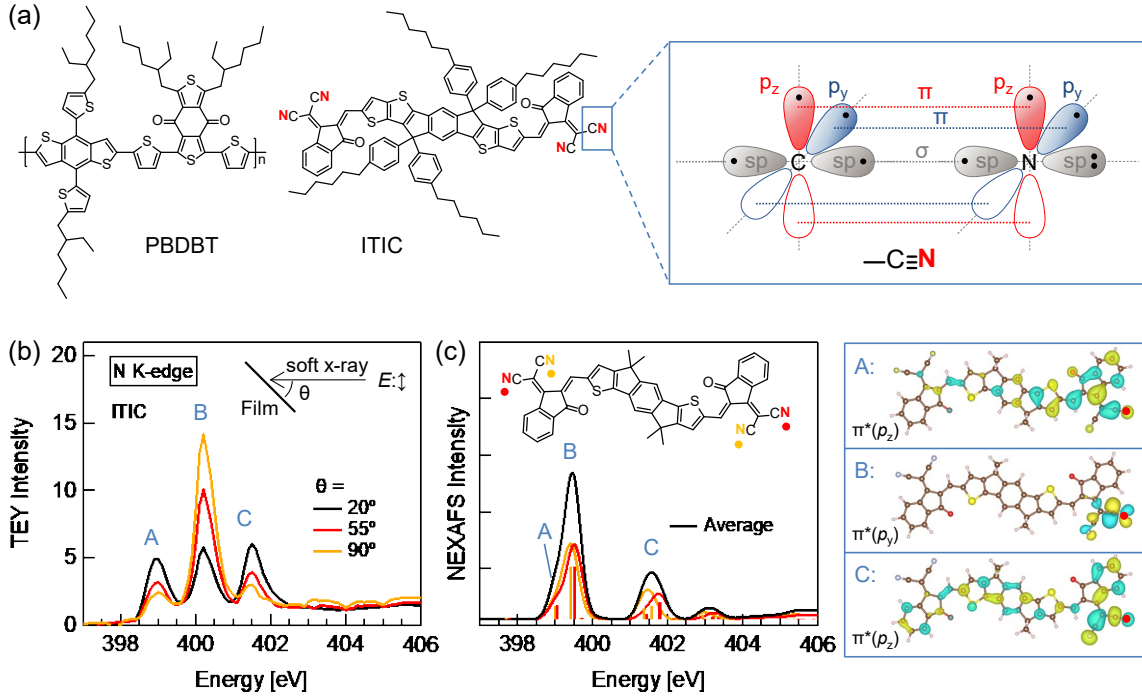


**Figure 1.** (a) Chemical structures of PBDBT and ITIC, where the cyano group of ITIC is formed with one  $\sigma$  bond and two  $\pi$  bonds. (b) Angle-dependent N K-edge NEXAFS spectra of ITIC; inset is the schematic showing the experimental geometry with beam incident angle of  $\theta$ , where the incident electric field ( $E$ ) is perpendicular to the sample. The NEXAFS spectra were collected with total electron yield (TEY) mode. (c) Left: simulated N K-edge NEXAFS spectra of the simplified ITIC. Right: density distributions of the electronic component of different core-excited final-state orbitals, where the excited N atoms are highlighted with red.

The determination of chemical origins for absorption peaks enables the structure analysis with NK-RSoXS. RSoXS was then performed on freestanding PBDBT:ITIC (1:1 by weight) blend film in transmission geometry to avoid the fluorescence background of silicon nitride ( $\text{Si}_3\text{N}_4$ ) supporting window or need to fabricate a nitrogen-free support like aluminum oxide substrate.<sup>42</sup> Figures 2a and 2b summarize the averaged RSoXS  $I-q$  curves collected at C K-edge and N K-edge, respectively. For CK-RSoXS, the blend film shows a peak with  $q \sim 0.012 \text{ \AA}^{-1}$  ( $d \sim 52 \text{ nm}$ ,  $d = 2\pi/q$ ) at 280.0 eV. When the photon energy is switched to the  $\pi^*$  resonance region (284.0 - 286.0 eV), a significantly enhanced peak with  $q$  position around  $0.0083 \text{ \AA}^{-1}$  ( $d \sim 75 \text{ nm}$ ) is seen (Figure S5). The emergence of multiple scattering peaks indicates CK-RSoXS can detect a complex nanostructure in the blend, but cannot well decipher the structural details with chemical specificity due to the overlapped NEXAFS spectra. When shifted to NK-RSoXS, a weak scattering feature is observed at  $0.0022 \text{ \AA}^{-1}$  ( $d \sim 285 \text{ nm}$ ) at off-resonance energies (390 eV and

408 eV). Tuning the photon energy to the three key resonant N 1s $\rightarrow\pi^*$  absorptions (398.8 eV, 400.2 eV, and 401.4 eV), scattering features are seen at 0.011 Å $^{-1}$  ( $d \sim 55$  nm) with different intensities, and the best resonance is seen at 400.0 eV, which is assigned to the peak B resonant absorption in NEXAFS (Figure S6). These results indicate that NK-RSoXS can clearly capture the N heterogeneity in blend, which is in consistence with the off-resonance CK RSoXS, indicating this structure feature originates from the ITIC crystalline phase in blends.

We then calculate the integrated scattering intensity (ISI) of RSoXS to evaluate the phase contrast following the equation of  $ISI = \int_0^\infty I(q)q^2 dq$ . For a two-phase system, the relationship between ISI and contrast function can be described by

$$ISI = 2\pi^2 \Delta\rho_{12}^2 \varphi_1 \varphi_2 V \propto \Delta\rho_{12}^2 \propto E^4 (\Delta\delta^2 + \Delta\beta^2)$$

where  $\Delta\rho_{12}$  is the difference in effective electron density of the two phases,  $\varphi_1$  and  $\varphi_2$  are the volume fractions of each phase, and  $V$  is the scattering volume.<sup>18,43</sup> Thus, the ISI is proportional to the contrast function  $\Delta\delta^2 + \Delta\beta^2$ . The acquisition of the NEXAFS spectra of the pure material enables to obtain the imaginary part of the refractive of index,  $\beta$ , for each material. Then the real part,  $\delta$ , can be calculated through the Kramers-Kronig relationship,<sup>44</sup> enabling the calculation of contrast between the materials in a blend. For the PBDBT:ITIC blend, the scattering contrast at C K-edge is dependent on the difference of index of refraction for each material ( $\Delta\delta^2 + \Delta\beta^2$ ), and the contrast at N K-edge is only affected by vacuum contrast of ITIC ( $\delta^2 + \beta^2$ ) since only ITIC has N atoms (Figures S10 and S11). The comparison of the experimental ISI and calculated contrast function reveals how the scattering power in RSoXS reflects the contrast between PBDBT and ITIC.

As shown in Figure 2c, the energy-dependent ISI at C K-edge shows dual-peak profile with large ISIs at 283.8 eV and 286.0 eV, which is not fully consistent with the calculated  $\Delta\delta^2 + \Delta\beta^2$ . This effect is ascribed to the orientation contrast in blends, which cannot be fully taken into account in contrast calculations based on orientation averaged NEXAFS. The scattering signal at 283.3 eV reflects the best resonance effect for PBDBT:ITIC blends. Close inspection of the 2D scattering pattern (inset in Figure 2a) shows that the scattering anisotropy is parallel with the  $E$  vector at low- $q$  region, which is different to the anisotropy feature perpendicular to  $E$  vector at high- $q$  region, indicating the scatters are of different origins. Sector averaging in the directions parallel and perpendicular to  $E$  was performed, resulting scattering features at 0.0081 Å $^{-1}$  ( $d \sim 78$  nm) and 0.0099 Å $^{-1}$  ( $d \sim 63$  nm), respectively, as indicated by their  $Iq^2-q$  curves (Figure S12). However, defining the chemical origins for these features is challenging due to the overlapped

NEXAFS features between PBDBT and ITIC around 283.8 eV (Figure S9). The ISI at N K-edge shows a profile matches well with the calculated  $\delta^2+\beta^2$ , which helps to find the clear origin of the  $0.011 \text{ \AA}^{-1}$  scattering ( $d \sim 55 \text{ nm}$ ) in NK-RSoXS, corresponding to the inter-distance of ITIC phase. This characteristic length is close to the small size observed by the CK-RSoXS ( $d \sim 63 \text{ nm}$ ), and thus the large size feature ( $d \sim 78 \text{ nm}$ ) in CK-RSoXS is ascribed to the PBDBT phase. A schematic representation is shown in Figure 2d. NK-RSoXS (400 eV) highlights specific features of the complex morphology associated with the cyano ITIC that cannot be easily determined with CK-RSoXS. This combination enables the decoupling of the complex multi-length-scale phase separated morphology in NFA blends for the first time. These results demonstrate that NK-RSoXS shows unique capability to explicitly highlight the cyano NFAs, which is complementary to the CK-RSoXS, realizing new opportunities to investigate the complex morphology and construct the structure-property relationship in high efficiency NFA solar cells.

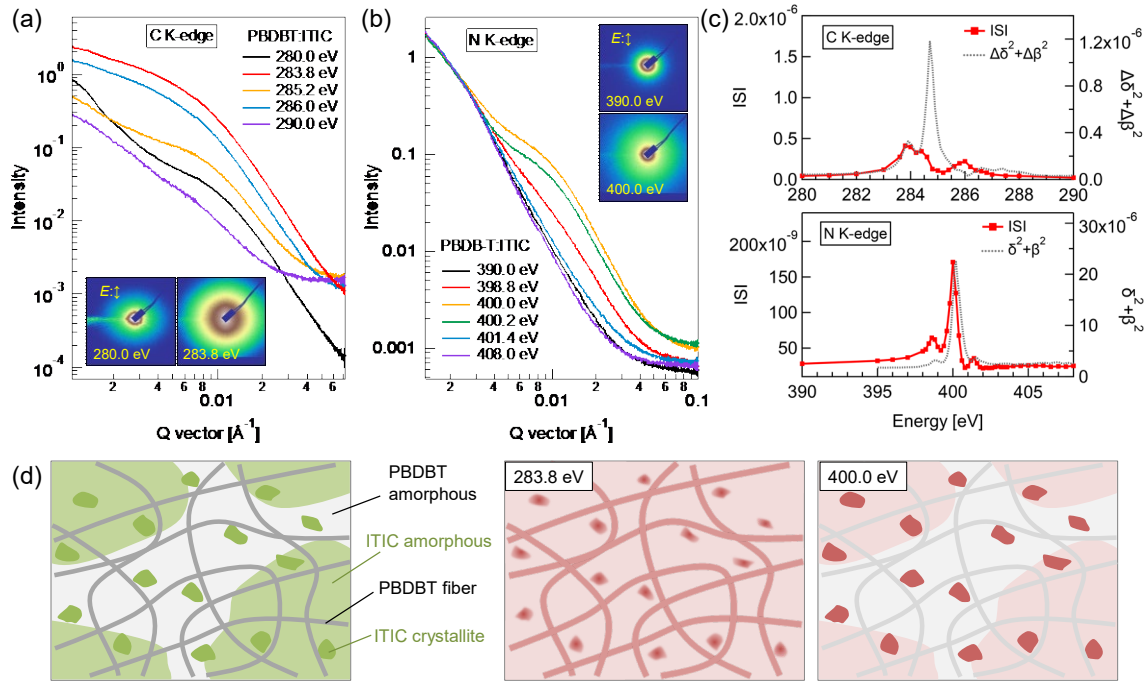


**Figure 2.** Energy-dependent (a) CK- and (b) NK-RSoXS averaged  $I-q$  curves of PBDBT:ITIC blend film; insets are the scattering patterns of off-resonance (C K-edge: 280.0 eV; N K-edge: 390.0 eV) and on-resonance (C K-edge: 284.0 eV; N K-edge: 400.0 eV) energies. (c) ISI as a function of energy and the predicted contrast functions,  $\Delta\delta^2 + \Delta\beta^2$  for C K-edge and  $\delta^2 + \beta^2$  for N K-edge, of the PBDBT:ITIC blend film. The  $q$  ranges for ISI calculations were set to 0.0011-0.024 Å<sup>-1</sup> for NK-RSOXS and 0.0040-0.033 Å<sup>-1</sup> for CK-RSoXS to minimize the fluorescence background at high scattering angle. (d) Schematic showing the morphology of PBDBT:ITIC

blend, with PBDBT fibers, ITIC crystallites, and phase separation of amorphous domains (left), and the structures highlighted by soft x-rays with energies at 283.8 eV (C K-edge, middle) and 400.0 eV (N K-edge, right).

We then look into the record-holding PM6:Y6 OPV blends, which exhibit solar cell efficiency over 17% (Figure 3a).<sup>45</sup> As shown in Figure 3b, the cyano Y6 acceptor shows three N 1s→π\* transition peaks in NEXAFS spectra. Although the simulated spectra also shows three transition features from the cyano groups, the presence of transitions from the N atoms in the central hetero-aromatic rings complicates the assignment of the TDMs for each peak in the experimental data (Figure S13). Similar to ITIC, the three NEXAFS features of Y6 are also labeled by “A”, “B”, and “C”. Angle-dependent spectra shows that decreasing the incident angle  $\theta$  from 90° to 20° leads to significantly intensified peaks A and C, but declined peak B. The similar NEXAFS dichroism compared with ITIC suggests that the peak B is mainly contributed by the N 1s→π\* transition with TDM within the conjugated plane, while peaks A and C are mainly contributed by the N 1s→π\* transitions with TDMs normal to the conjugated plane.

The NK-RSoXS  $I\text{-}q$  curves of PM6:Y6 blend (1:1.2 by weight) is shown in Figure 3c. Well-defined dual-peak characteristics are recorded with one center at 0.0048 Å<sup>-1</sup> ( $d \sim 147$  nm) and another at 0.016 Å<sup>-1</sup> ( $d \sim 37$  nm), both of which are associated with the Y6 phase, as their scattering intensities vary with the photon energy at N K-edge, indicating that Y6 presents multi-length-scale phase separation in the blend (Figures S14 and S15). To study the origin of the two scattering features, ISIs at high- $q$  region and low- $q$  region are calculated (Figure 3d). The high- $q$  ISI profile is dominated by peak B, suggesting that the chemical resonance mainly comes from the N 1s→π\* transitions with TDMs in the Y6 conjugated plane, which agrees with the “face-on” orientation of Y6. For the low- $q$  ISI profile, peak C shows comparable intensity to peaks A and B, implying that the chemical resonance is contributed by N 1s→π\* transitions with TDMs not only within but also normal to the Y6 plane, which fits in the amorphous mixture region where the Y6 molecules has little orientation preference. It has been shown that Y6 in PM6:Y6 blend forms crystallite fiber morphology, where molecules assume preferential “face-on” orientation.<sup>46</sup> The energy-dependent ISI analysis together with the self-assembly structure suggests that the scattering resonance at high- $q$  region comes from the Y6 fiber inter-distance (~37 nm), which is in good agreement with the results observed in AFM phase images (Figure S16). The scattering resonance at low- $q$  region originates from the Y6-rich amorphous region, a structure feature that has not been resolved before. Thus, NK-RSoXS successfully decoupled the complex multi-length-scale morphology arising from Y6 in PM6:Y6 blends, with the fiber network determined

by molecular crystallization and the amorphous domains formed from spinodal decomposition (Figure 3e).

With NK-RSoXS, a more complex ternary blend of PM6:Y6:Y6-BO (1:0.6:0.6 by weight) was studied to understand how the acceptor based multi-length-scale phase separation correlates with the photovoltaic performance (Figure S14). Analysis of the energy-dependent  $I$ - $q$  curves and ISI reveals that the ternary blend has NK-RSoXS peaks at  $0.0048 \text{ \AA}^{-1}$  and  $0.016 \text{ \AA}^{-1}$ , indicating the inter-distances of amorphous domains and crystallite fibers are 131 nm and 39 nm, respectively (Figures S17-S19). Thus, the major change in this ternary blend is the reduced distance of amorphous domains of acceptors, from 147 nm to 131 nm compared with the PM6:Y6 blend. As a result, more efficient exciton diffusion and dissociation, as well as substantial current amplification for the ternary solar cells are observed.<sup>46</sup> These results indicate that the complex structures arising from cyano acceptors decoupled by NK-RSoXS can help to understand the device performance outcomes, providing new understanding of structure-property relationship. The device performances and the key charge transfer and carrier transport properties are summarized in Figure S27 and Table S1. We see clearly that the PM6:Y6:Y6-BO blend delivers a higher short-circuit current ( $J_{SC}$ ) by ~4% and a slightly improved fill factors. These results are in accordance with the reduced amorphous phase separation as probed by NK-RSoXS. It is also noticed that the charge dissociation in mixed region is much shorter and the electron mobility is higher in PM6:Y6:Y6-BO blends, which are ascribed to the reduced phase separation and enhanced crystallization for acceptor components.

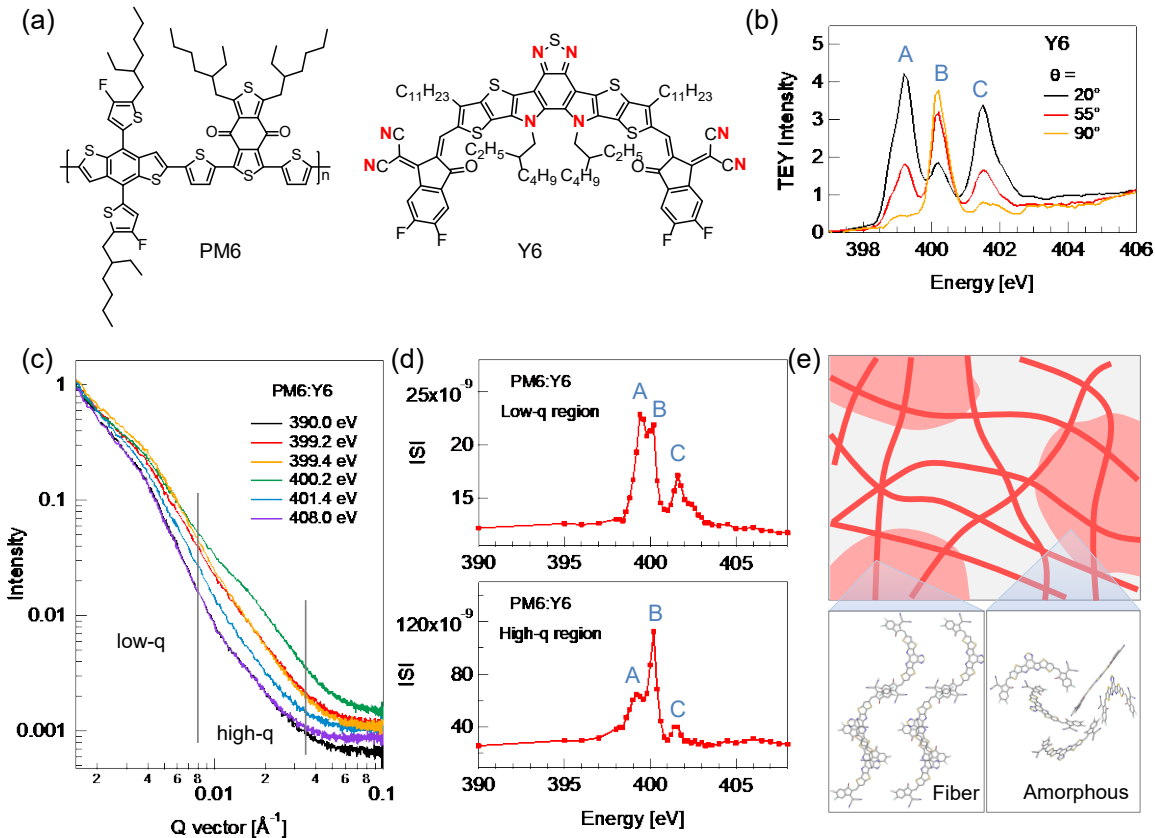


**Figure 3.** (a) Chemical structures of PM6 and Y6. (b) Angle-dependent N K-edge NEXAFS spectra of Y6, which were collected with TEY mode. (c) Energy-dependent NK-RSoXS averaged curves of PM6:Y6 (1:1.2) blend films. (d) ISIs as a function of energy of PM6:Y6 blend; the high- $q$  and low- $q$  regions are 0.0012–0.0080  $\text{\AA}^{-1}$  and 0.0080–0.036  $\text{\AA}^{-1}$ , respectively. (e) Schematic showing the complex multi-length-scale phase separation with Y6 crystallite fibers interpenetrating through the Y6 amorphous regions, where the molecular packing assumes “face-on” orientation in crystallite fibers but random orientation in amorphous regions.

Furthermore, angle-dependent N K-edge NEXAFS for several representative  $\pi$ -conjugated materials with N-based hetero-aromatic rings and cyano groups are collected in Figure 4, which are widely used in various types of organic electronics.<sup>47–60</sup> Taking their significant N 1s  $\rightarrow \pi^*$  resonances, NK-RSoXS is promising to be applied in resolving the complex structures to construct a solid structure-property relationship for a broad range of organic semiconductor thin films. Therefore, for a blend, where one or several components contain N with distinguishable 1s  $\rightarrow \pi^*$  resonances, the N atoms can be used as the tracer to track the morphology with chemical specificity by using NK-RSoXS, which provides a similar effect to deuterium labeling in small angle neutral scattering (SANS). Angle-dependent NEXAFS of the listed materials are provided

for reference, which provides essential information regarding the orientation of scattering entities in a sample and is critical in analyzing the scattering results. Thus, NK-RSoXS provides a simple but effective solution to decipher structural complexity and study the mesoscale behaviors in functional soft materials.

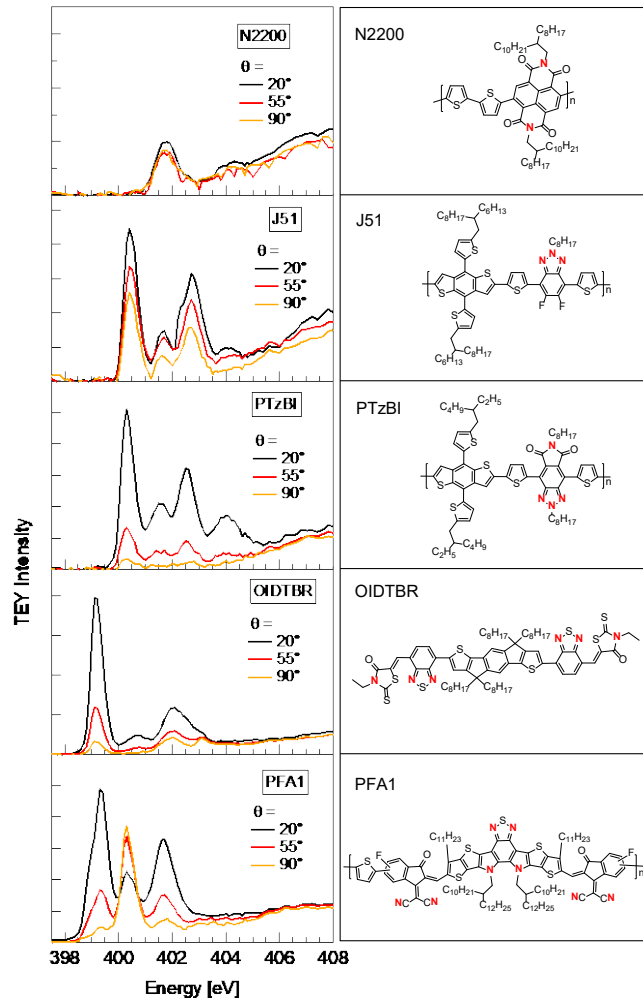


**Figure 4.** Angle-dependent N K-edge NEXAFS spectra (TEY mode, left) and chemical structures (right) of N2200,<sup>47</sup> J51,<sup>48,49</sup> PTzBI,<sup>50</sup> OIDTBR,<sup>51,52</sup> and PFA1<sup>53</sup>.

## CONCLUSION

We demonstrate the capability of NK-RSoXS in resolving the complex morphology in non-fullerene solar cell blends, which turns out to be a successful avenue in studying the multi-length-scale morphology stemming from material crystallization and phase separation. The cyano group

in non-fullerene acceptors with distinct N 1s→π\* resonances provides an ideal label, by which the material contrast and orientation factor can be used to decouple the complex morphology in the bulk-heterojunction blend. As seen in PM6:Y6 blends, Y6 crystallization and phase separation leads to crystallite fibrillar morphology and Y6 enriched amorphous domain that account for the high efficiency carrier generation and transportation in solar cell devices. The PM6:Y6:Y6-BO ternary blend shows reduced amorphous phase separation distance and improved crystallization, leading to improved electron mobility, charge separation, and short circuit current. In executing NK-RSoXS analysis, merging experimental and theoretical NEXAFS spectroscopy is crucial in correlating spectral features and scattering origins. The N K-edge NEXAFS spectra of representative materials based on N-containing hetero-aromatic rings and cyano groups are examined, showing strong resonances and dichroism, providing new opportunities for NK-RSoXS to unlock the complex phase separation for a broad range of organic semiconductor thin films. The unique capability of NK-RSoXS to highlight the N-containing heterogeneities provides a complementary tool to other characterization techniques,<sup>24,61,62</sup> and can enable unprecedented opportunities to glimpse into the chemical, spatial, and temporal behaviors of mesoscale complexity for functional soft materials in various application frontiers.

## ASSOCIATED CONTENT

### Supporting Information

The Supporting Information is available free of charge on the ACS Publications website.

## AUTHOR INFORMATION

### Corresponding Author

Feng Liu - *Frontiers Science Center for Transformative Molecules, In-situ Center for Physical Science, and Center of Hydrogen Science, School of Chemistry and Chemical Engineering, Shanghai Jiao Tong University, Shanghai 200240, China; orcid.org/0000-0002-5572-8512*

Email: fengliu82@sjtu.edu.cn

Cheng Wang - *Advanced Light Source, Lawrence Berkeley National Laboratory, Berkeley, CA 94720, United States; orcid.org/0000-0001-7192-5471*

Email: cwang2@lbl.gov

## Authors

Wenkai Zhong - *Frontiers Science Center for Transformative Molecules, In-situ Center for Physical Science, and Center of Hydrogen Science, School of Chemistry and Chemical Engineering, Shanghai Jiao Tong University, Shanghai 200240, China; Advanced Light Source, Lawrence Berkeley National Laboratory, Berkeley, CA 94720, United States; orcid.org/0000-0001-8333-4898*

Ming Zhang - *Frontiers Science Center for Transformative Molecules, In-situ Center for Physical Science, and Center of Hydrogen Science, School of Chemistry and Chemical Engineering, Shanghai Jiao Tong University, Shanghai 200240, China*

Guillaume Freychet - *NSLS-II, Brookhaven National Laboratory, Upton, New York 11973, United States*

Gregory M. Su - *Advanced Light Source and Materials Sciences Division, Lawrence Berkeley National Laboratory, Berkeley, CA 94720, United States; orcid.org/0000-0001-7495-8041*

Lei Ying - *Institute of Polymer Optoelectronic Materials and Devices, State Key Laboratory of Luminescent Materials and Devices, South China University of Technology, Guangzhou 510640, China*

Fei Huang - *Institute of Polymer Optoelectronic Materials and Devices, State Key Laboratory of Luminescent Materials and Devices, South China University of Technology, Guangzhou 510640, China*

Yong Cao - *Institute of Polymer Optoelectronic Materials and Devices, State Key Laboratory of Luminescent Materials and Devices, South China University of Technology, Guangzhou 510640, China*

Yongming Zhang - *Frontiers Science Center for Transformative Molecules, In-situ Center for Physical Science, and Center of Hydrogen Science, School of Chemistry and Chemical Engineering, Shanghai Jiao Tong University, Shanghai 200240, China*

## Notes

The authors declare no competing financial interest.

## ACKNOWLEDGMENTS

This research used resources of the Advanced Light Source and the Molecular Foundry, Lawrence Berkeley National Laboratory, which were supported by the Office of Science, Office of Basic Energy Sciences, of the U.S. Department of Energy under Contract No. DE-AC02-05CH11231.

## REFERENCES

- (1) US Department of Energy Basic Energy Science Report, “From Quanta to the Continuum: Opportunities for Mesoscale Science (September, 2012)”: <https://doi.org/10.2172/1183982>.
- (2) Sarrao, J. L.; Crabtree, G. W. Opportunities and advances in mesoscale science. *Curr. Opin. Solid State Mater. Sci.* **2015**, *19*, 201-202.
- (3) Wang, C.; Lee, D. H.; Hexemer, A.; Kim, M. I.; Zhao, W.; Hasegawa, H.; Ade, H.; Russell, T. P. Defining the Nanostructured Morphology of Triblock Copolymers Using Resonant Soft X-ray Scattering. *Nano Lett.* **2011**, *11*, 3906-3911.
- (4) Ye, D.; Kiemle, S. N.; Rongpipi, S.; Wang, X.; Wang, C.; Cosgrove, D. J.; Gomez, E. W.; Gomez, E. D. Resonant soft X-ray scattering reveals cellulose microfibril spacing in plant primary cell walls. *Sci. Rep.* **2018**, *8*, 12449.
- (5) Ye, D.; Le, T. P.; Kuei, B.; Zhu, C.; Zwart, P. H.; Wang, C.; Gomez, E. D.; Gomez, E. W. Resonant Soft X-Ray Scattering Provides Protein Structure with Chemical Specificity. *Structure* **2018**, *26*, 1513-1521.e3.
- (6) Zhu, C.; Wang, C.; Young, A.; Liu, F.; Gunkel, I.; Chen, D.; Walba, D.; MacLennan, J.; Clark, N.; Hexemer, A. Probing and Controlling Liquid Crystal Helical Nanofilaments. *Nano Lett.* **2015**, *15*, 3420-3424.
- (7) Su, G. M.; Cordova, I. A.; Wang, C. New Insights into Water Treatment Materials with Chemically Sensitive Soft and Tender X-rays. *Synchrotron Radiat. News* **2020**, *33*, 17-23.
- (8) McAfee, T.; Ferron, T.; Cordova, I. A.; Pickett, P. D.; McCormick, C. L.; Wang, C.; Collins, B. A. Label-free characterization of organic nanocarriers reveals persistent single molecule cores for hydrocarbon sequestration. *Nat. Comm.* **2021**, *12*, 3123.
- (9) Liu, F.; Brady, M. A.; Wang, C. Resonant soft X-ray scattering for polymer materials. *Eur. Polym. J.* **2016**, *81*, 555-568.
- (10) Zhong, W.; Liu, F.; Wang, C. Probing morphology and chemistry in complex soft materials with in situ resonant soft x-ray scattering. *J. Phys. Condens. Matter* **2021**, *33*, 313001.

- (11) Gann, E.; Young, A. T.; Collins, B. A.; Yan, H.; Nasiatka, J.; Padmore, H. A.; Ade, H.; Hexemer, A.; Wang, C. Soft x-ray scattering facility at the Advanced Light Source with real-time data processing and analysis. *Rev. Sci. Instrum.* **2012**, *83*, 045110.
- (12) Rivnay, J.; Mannsfeld, S. C. B.; Miller, C. E.; Salleo, A.; Toney, M. F. Quantitative Determination of Organic Semiconductor Microstructure from the Molecular to Device Scale. *Chem. Rev.* **2012**, *112*, 5488-5519.
- (13) Huang, Y.; Kramer, E. J.; Heeger, A. J.; Bazan, G. C. Bulk Heterojunction Solar Cells: Morphology and Performance Relationships. *Chem. Rev.* **2014**, *114*, 7006-7043.
- (14) Liu, F.; Gu, Y.; Shen, X.; Ferdous, S.; Wang, H.-W.; Russell, T. P. Characterization of the morphology of solution-processed bulk heterojunction organic photovoltaics. *Prog. Polym. Sci.* **2013**, *38*, 1990-2052.
- (15) Collins, B. A.; Cochran, J. E.; Yan, H.; Gann, E.; Hub, C.; Fink, R.; Wang, C.; Schuettfort, T.; McNeill, C. R.; Chabinyc, M. L.; Ade, H. Polarized X-ray scattering reveals non-crystalline orientational ordering in organic films. *Nat. Mater.* **2012**, *11*, 536-543.
- (16) Tumbleston, J. R.; Collins, B. A.; Yang, L.; Stuart, A. C.; Gann, E.; Ma, W.; You, W.; Ade, H. The influence of molecular orientation on organic bulk heterojunction solar cells. *Nat. Photonics* **2014**, *8*, 385-391.
- (17) Liu, F.; Wang, C.; Baral, J. K.; Zhang, L.; Watkins, J. J.; Briseno, A. L.; Russell, T. P. Relating Chemical Structure to Device Performance via Morphology Control in Diketopyrrolopyrrole-Based Low Band Gap Polymers. *J. Am. Chem. Soc.* **2013**, *135*, 19248-19259.
- (18) Collins, B. A.; Li, Z.; Tumbleston, J. R.; Gann, E.; McNeill, C. R.; Ade, H. Absolute Measurement of Domain Composition and Nanoscale Size Distribution Explains Performance in PTB7:PC71BM Solar Cells. *Adv. Energy Mater.* **2013**, *3*, 65-74.
- (19) Hou, J.; Inganäs, O.; Friend, R. H.; Gao, F. Organic solar cells based on non-fullerene acceptors. *Nat. Mater.* **2018**, *17*, 119-128.
- (20) Yan, C.; Barlow, S.; Wang, Z.; Yan, H.; Jen, A. K. Y.; Marder, S. R.; Zhan, X. Non-fullerene acceptors for organic solar cells. *Nat. Rev. Mater.* **2018**, *3*, 18003.
- (21) Zhu, L.; Zhang, M.; Zhong, W.; Leng, S.; Zhou, G.; Zou, Y.; Su, X.; Ding, H.; Gu, P.; Liu, F.; Zhang, Y. Progress and prospects of the morphology of non-fullerene acceptor based high-efficiency organic solar cells. *Energy Environ. Sci.* **2021**, DOI: 10.1039/D1EE01220G.
- (22) Fu, H.; Wang, Z.; Sun, Y. Polymer Donors for High-Performance Non-Fullerene Organic Solar Cells. *Angew. Chem. Int. Ed.* **2019**, *58*, 4442-4453.

- (23) Liu, W.; Xu, X.; Yuan, J.; Leclerc, M.; Zou, Y.; Li, Y. Low-Bandgap Non-fullerene Acceptors Enabling High-Performance Organic Solar Cells. *ACS Energy Lett.* **2021**, *6*, 598-608.
- (24) Gu, K. L.; Zhou, Y.; Morrison, W. A.; Park, K.; Park, S.; Bao, Z. Nanoscale Domain Imaging of All-Polymer Organic Solar Cells by Photo-Induced Force Microscopy. *ACS Nano* **2018**, *12*, 1473-1481.
- (25) Cheng, Y.-J.; Yang, S.-H.; Hsu, C.-S. Synthesis of Conjugated Polymers for Organic Solar Cell Applications. *Chem. Rev.* **2009**, *109*, 5868-5923.
- (26) Blouin, N.; Michaud, A.; Gendron, D.; Wakim, S.; Blair, E.; Neagu-Plesu, R.; Belletête, M.; Durocher, G.; Tao, Y.; Leclerc, M. Toward a Rational Design of Poly(2,7-Carbazole) Derivatives for Solar Cells. *J. Am. Chem. Soc.* **2008**, *130*, 732-742
- (27) Price, S. C.; Stuart, A. C.; Yang, L.; Zhou, H.; You, W. Fluorine Substituted Conjugated Polymer of Medium Band Gap Yields 7% Efficiency in Polymer–Fullerene Solar Cells. *J. Am. Chem. Soc.* **2011**, *133*, 4625-4631.
- (28) Zhou, H.; Yang, L.; Price, S. C.; Knight, K. J.; You, W. Enhanced Photovoltaic Performance of Low-Bandgap Polymers with Deep LUMO Levels. *Angew. Chem. Int. Ed.* **2010**, *49*, 7992-7995.
- (29) Welch, G. C.; Coffin, R.; Peet, J.; Bazan, G. C. Band Gap Control in Conjugated Oligomers via Lewis Acids. *J. Am. Chem. Soc.* **2009**, *131*, 10802-10803.
- (30) Welch, G. C.; Bazan, G. C. Lewis Acid Adducts of Narrow Band Gap Conjugated Polymers. *J. Am. Chem. Soc.* **2011**, *133*, 4632-4644.
- (31) Liu, F.; Zhou, Z.; Zhang, C.; Vergote, T.; Fan, H.; Zhu, X. A Thieno[3,4-b]thiophene-Based Non-fullerene Electron Acceptor for High-Performance Bulk-Heterojunction Organic Solar Cells. *J. Am. Chem. Soc.* **2016**, *138*, 15523-15526.
- (32) Chen, Y.; Zheng, Y.; Jiang, Y.; Fan, H.; Zhu, X. Carbon-Bridged 1,2-Bis(2-thienyl)ethylene: An Extremely Electron Rich Dithiophene Building Block Enabling Electron Acceptors with Absorption above 1000 nm for Highly Sensitive NIR Photodetectors. *J. Am. Chem. Soc.* **2021**, *143*, 4281-4289.
- (33) Kan, B.; Li, M.; Zhang, Q.; Liu, F.; Wan, X.; Wang, Y.; Ni, W.; Long, G.; Yang, X.; Feng, H.; Zuo, Y.; Zhang, M.; Huang, F.; Cao, Y.; Russell, T. P.; Chen, Y. A Series of Simple Oligomer-like Small Molecules Based on Oligothiophenes for Solution-Processed Solar Cells with High Efficiency. *J. Am. Chem. Soc.* **2015**, *137*, 3886-3893.
- (34) Zhang, Q.; Kan, B.; Liu, F.; Long, G.; Wan, X.; Chen, X.; Zuo, Y.; Ni, W.; Zhang, H.; Li, M.; Hu, Z.; Huang, F.; Cao, Y.; Liang, Z.; Zhang, M.; Russell, T. P.; Chen, Y. Small-molecule solar cells with efficiency over 9%. *Nat. Photonics* **2015**, *9*, 35-41.

- (35) Li, C.; Zhou, J.; Song, J.; Xu, J.; Zhang, H.; Zhang, X.; Guo, J.; Zhu, L.; Wei, D.; Han, G.; Min, J.; Zhang, Y.; Xie, Z.; Yi, Y.; Yan, H.; Gao, F.; Liu, F.; Sun, Y. Non-fullerene acceptors with branched side chains and improved molecular packing to exceed 18% efficiency in organic solar cells. *Nat. Energy* **2021**, *6*, 605-613.
- (36) Guo, Q.; Ma, R.; Hu, J.; Wang, Z.; Sun, H.; Dong, X.; Luo, Z.; Liu, T.; Guo, X.; Guo, X.; Yan, H.; Liu, F.; Zhang, M. Over 15% Efficiency Polymer Solar Cells Enabled by Conformation Tuning of Newly Designed Asymmetric Small-Molecule Acceptors. *Adv. Funct. Mater.* **2020**, *30*, 2000383.
- (37) Zhao, W.; Qian, D.; Zhang, S.; Li, S.; Inganäs, O.; Gao, F.; Hou, J. Fullerene-Free Polymer Solar Cells with over 11% Efficiency and Excellent Thermal Stability. *Adv. Mater.* **2016**, *28*, 4734-4739.
- (38) Yang, Y.; Zhang, Z.-G.; Bin, H.; Chen, S.; Gao, L.; Xue, L.; Yang, C.; Li, Y. Side-Chain Isomerization on an n-type Organic Semiconductor ITIC Acceptor Makes 11.77% High Efficiency Polymer Solar Cells. *J. Am. Chem. Soc.* **2016**, *138*, 15011-15018.
- (39) Xiao, L.; He, B.; Hu, Q.; Maserati, L.; Zhao, Y.; Yang, B.; Kolaczkowski, M. A.; Anderson, C. L.; Borys, N. J.; Klivansky, L. M.; Chen, T. L.; Schwartzberg, A. M.; Russell, T. P.; Cao, Y.; Peng, X.; Liu, Y. Multiple Roles of a Non-fullerene Acceptor Contribute Synergistically for High-Efficiency Ternary Organic Photovoltaics. *Joule* **2018**, *2*, 2154-2166.
- (40) Prendergast, D.; Galli, G. X-Ray Absorption Spectra of Water from First Principles Calculations. *Phys. Rev. Lett.* **2006**, *96*, 215502.
- (41) Su, G. M.; Patel, S. N.; Pemmaraju, C. D.; Prendergast, D.; Chabinyc, M. L. First-Principles Predictions of Near-Edge X-ray Absorption Fine Structure Spectra of Semiconducting Polymers. *J. Phys. Chem. C* **2017**, *121*, 9142-9152.
- (42) Ye, D.; Rongpipi, S.; Litofsky, J. H.; Lee, Y.; Culp, T. E.; Yoo, S. H.; Jackson, T. N.; Wang, C.; Gomez, E. W.; Gomez, E. D. Aluminum oxide free-standing thin films to enable nitrogen edge soft x-ray scattering. *MRS Commun.* **2019**, *9*, 224-228.
- (43) Glatter, O.; Kratky, O. Small Angle X-Ray Scattering; Academic Press, New York, **1982**.
- (44) Watts, B. Calculation of the Kramers-Kronig transform of X-ray spectra by a piecewise Laurent polynomial method. *Opt. Express* **2014**, *22*, 23628-23639.
- (45) Zhu, L.; Zhang, M.; Zhou, G.; Hao, T.; Xu, J.; Wang, J.; Qiu, C.; Prine, N.; Ali, J.; Feng, W.; Gu, X.; Ma, Z.; Tang, Z.; Zhu, H.; Ying, L.; Zhang, Y.; Liu, F. Efficient Organic Solar Cell with 16.88% Efficiency Enabled by Refined Acceptor Crystallization and Morphology with Improved Charge Transfer and Transport Properties. *Adv. Energy Mater.* **2020**, *10*, 1904234.

- (46) Zhang, M.; Zhu, L.; Hao, T.; Zhou, G.; Qiu, C.; Zhao, Z.; Hartmann, N.; Xiao, B.; Zou, Y.; Feng, W.; Zhu, H.; Zhang, M.; Zhang, Y.; Li, Y.; Russell, T. P.; Liu, F. High-Efficiency Organic Photovoltaics using Eutectic Acceptor Fibrils to Achieve Current Amplification. *Adv. Mater.* **2021**, *33*, 2007177.
- (47) Yan, H.; Chen, Z.; Zheng, Y.; Newman, C.; Quinn, J. R.; Dötz, F.; Kastler, M.; Facchetti, A. A high-mobility electron-transporting polymer for printed transistors. *Nature* **2009**, *457*, 679-686.
- (48) Gao, L.; Zhang, Z.-G.; Bin, H.; Xue, L.; Yang, Y.; Wang, C.; Liu, F.; Russell, T. P.; Li, Y. High-Efficiency Nonfullerene Polymer Solar Cells with Medium Bandgap Polymer Donor and Narrow Bandgap Organic Semiconductor Acceptor. *Adv. Mater.* **2016**, *28*, 8288-8295.
- (49) Gao, L.; Zhang, Z.-G.; Xue, L.; Min, J.; Zhang, J.; Wei, Z.; Li, Y. All-Polymer Solar Cells Based on Absorption-Complementary Polymer Donor and Acceptor with High Power Conversion Efficiency of 8.27%. *Adv. Mater.* **2016**, *28*, 1884-1890.
- (50) Fan, B. B.; Ying, L.; Wang, Z. F.; He, B. T.; Jiang, X. F.; Huang, F.; Cao, Y. Optimisation of processing solvent and molecular weight for the production of green-solvent-processed all-polymer solar cells with a power conversion efficiency over 9%. *Energy Environ. Sci.* **2017**, *10*, 1243-1251.
- (51) Holliday, S.; Ashraf, R. S.; Wadsworth, A.; Baran, D.; Yousaf, S. A.; Nielsen, C. B.; Tan, C.-H.; Dimitrov, S. D.; Shang, Z.; Gasparini, N.; Alamoudi, M.; Laquai, F.; Brabec, C. J.; Salleo, A.; Durrant, J. R.; McCulloch, I. High-efficiency and air-stable P3HT-based polymer solar cells with a new non-fullerene acceptor. *Nat. Comm.* **2016**, *7*, 11585.
- (52) Bristow, H.; Thorley, K. J.; White, A. J. P.; Wadsworth, A.; Babics, M.; Hamid, Z.; Zhang, W.; Paterson, A. F.; Kosco, J.; Panidi, J.; Anthopoulos, T. D.; McCulloch, I. Impact of Nonfullerene Acceptor Side Chain Variation on Transistor Mobility. *Adv. Electron. Mater.* **2019**, *5*, 1900344.
- (53) Peng, F.; An, K.; Zhong, W.; Li, Z.; Ying, L.; Li, N.; Huang, Z.; Zhu, C.; Fan, B.; Huang, F.; Cao, Y. A Universal Fluorinated Polymer Acceptor Enables All-Polymer Solar Cells with >15% Efficiency. *ACS Energy Lett.* **2020**, *5*, 3702-3707.
- (54) Fan, Q.; Fu, H.; Wu, Q.; Wu, Z.; Lin, F.; Zhu, Z.; Min, J.; Woo, H. Y.; Jen, A. K. Y. Multi-Selenophene-Containing Narrow Bandgap Polymer Acceptors for All-Polymer Solar Cells with over 15 % Efficiency and High Reproducibility. *Angew. Chem. Int. Ed.* **2021**, *60*, 15935-15943.
- (55) Fu, H.; Li, Y.; Yu, J.; Wu, Z.; Fan, Q.; Lin, F.; Woo, H. Y.; Gao, F.; Zhu, Z.; Jen, A. K. Y. High Efficiency (15.8%) All-Polymer Solar Cells Enabled by a Regioregular Narrow Bandgap Polymer Acceptor. *J. Am. Chem. Soc.* **2021**, *143*, 2665-2670.

- (56) Fan, B.; Du, X.; Liu, F.; Zhong, W.; Ying, L.; Xie, R.; Tang, X.; An, K.; Xin, J.; Li, N.; Ma, W.; Brabec, C. J.; Huang, F.; Cao, Y. Fine-tuning of the chemical structure of photoactive materials for highly efficient organic photovoltaics. *Nat. Energy* **2018**, *3*, 1051-1058.
- (57) Zhong, Y.; Causa', M.; Moore, G. J.; Krauspe, P.; Xiao, B.; Günther, F.; Kublitski, J.; Shihhare, R.; Benduhn, J.; BarOr, E.; Mukherjee, S.; Yallum, K. M.; Réhault, J.; Mannsfeld, S. C. B.; Neher, D.; Richter, L. J.; DeLongchamp, D. M.; Ortmann, F.; Vandewal, K.; Zhou, E.; Banerji, N. Sub-picosecond charge-transfer at near-zero driving force in polymer:non-fullerene acceptor blends and bilayers. *Nat. Comm.* **2020**, *11*, 833.
- (58) Sun, Y.; Welch, G. C.; Leong, W. L.; Takacs, C. J.; Bazan, G. C.; Heeger, A. J. Solution-processed small-molecule solar cells with 6.7% efficiency. *Nat. Mater.* **2012**, *11*, 44-48.
- (59) Jin, Y.; Chen, Z.; Dong, S.; Zheng, N.; Ying, L.; Jiang, X.-F.; Liu, F.; Huang, F.; Cao, Y. A Novel Naphtho[1,2-c:5,6-c']Bis([1,2,5]Thiadiazole)-Based Narrow-Bandgap  $\pi$ -Conjugated Polymer with Power Conversion Efficiency Over 10%. *Adv. Mater.* **2016**, *28*, 9811-9818.
- (60) Zhong, W.; Cui, J.; Fan, B.; Ying, L.; Wang, Y.; Wang, X.; Zhang, G.; Jiang, X.-F.; Huang, F.; Cao, Y. Enhanced Photovoltaic Performance of Ternary Polymer Solar Cells by Incorporation of a Narrow-Bandgap Nonfullerene Acceptor. *Chem. Mater.* **2017**, *29*, 8177-8186.
- (61) Su, G. M.; Cordova, I. A.; Brady, M. A.; Prendergast, D.; Wang, C. Combining theory and experiment for X-ray absorption spectroscopy and resonant X-ray scattering characterization of polymers. *Polymer* **2016**, *99*, 782-796.
- (62) Freychet, G.; Gann, E.; Thomsen, L.; Jiao, X.; McNeill, C. R. Resonant Tender X-ray Diffraction for Disclosing the Molecular Packing of Paracrystalline Conjugated Polymer Films. *J. Am. Chem. Soc.* **2021**, *143*, 1409-1415.

## Graphic Abstract

